Supporting Information

Near-infrared high-resolution imaging via deep learning based on broadband achromatic metalens

Lv-Rong Zhao, Lu Chen, Xiao-Qiang Jiang, Shao-Xiang Gong, Bo Gao, Huang-Rong Xu, and Wei-Xing Yu

Supplementary Section 1: Schematic of overall vertical shift of phase profiles

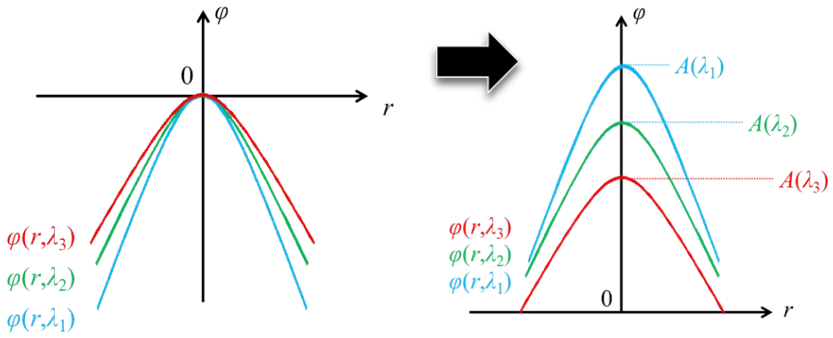

Fig. S1. Schematic of multi-wavelength achromatic phase function optimization

To determine the ideal target focusing phase for the achromatic metalens at each sampled wavelength, a bias function $A(\lambda)$ can be incorporated into the hyperbolic phase profile, as illustrated in Figure S1. This additional term $A(\lambda)$ shifts the hyperbolic focusing phase along the longitudinal direction, thereby satisfying the matching condition between the meta-atoms and the target focusing phases at the five discrete wavelength points. It is important to note that the relative phase distribution across different spatial locations remains consistent for each frequency, ensuring the focal position remains unaffected. In contrast to continuous-wavelength achromatic metalens design strategies, the discrete multi-wavelength approach eliminates the need to enforce a Linear phase–wavelength relationship, thus significantly simplifying the design process. Furthermore, the sampling interval adopted here is relatively narrow (less than 4.5% of the central wavelength), enabling achromatic focusing across the entire operational band, since each discrete wavelength point exhibits a certain phase bandwidth.

Supplementary Section 2: Sweeping range of the meta-atoms

By adjusting the geometric parameters of the meta-atoms, the meta-atom library can be obtained. And the detailed sweeping range of the six meta-atoms are listed in Table S1.

Table S1. Detailed sweeping range of the six meta-atoms.

Structure prototypes	Parameters	Variation range	Step length	Other constraints
Cylindrical	radius l_1	50 − 275 nm	2.5 nm	-
Concentric cylindrical	outer circle radius l_2	200 − 275 nm	2.5 nm	$l_2 - l_3 \geqq$ 100 nm
	inner circle radius l_3	100 − 175 nm	2.5 nm	
Cross-shaped	length m_1	100 − 550 nm	5.0 nm	$\lvert m_1 - m_2 \rvert \geqq$ 200 nm
	width m_2	100 − 550 nm	5.0 nm	
Cross-hole-shaped	outer square length m_0	550 nm	-	$\lvert m_3 - m_4 \rvert \geqq$ 200 nm
	length m_3	100 − 350 nm	5.0 nm	
	width m_4	100 − 350 nm	5.0 nm	
Square	length m_5	100 − 550nm	5.0 nm	-
Concentric-hole	outer square length m_0	550nm	-	-
	inner square length m_6	100 − 350 nm	5.0 nm	

Supplementary Section 3: The workflow diagram of PSO algorithm

As a leading global optimization technique in machine learning, the particle swarm optimization (PSO) algorithm is inspired by the social foraging behavior of bird flocks. It is known for its ease of implementation, high precision, and rapid convergence. The algorithm begins by initializing a population of random solutions, referred to as particles. During iterative search, each particle adjusts its trajectory based on two key factors: its own historically best solution (individual optimum) and the best solution found by any particle in the swarm (global optimum). This collaborative mechanism facilitates efficient exploration of the solution space. By continuously updating the velocity and position of each particle, PSO progresses toward the global optimum. The process terminates when either the desired performance criteria are satisfied or the maximum number of iterations is reached. And the workflow diagram of PSO is depicted in Fig. S2.

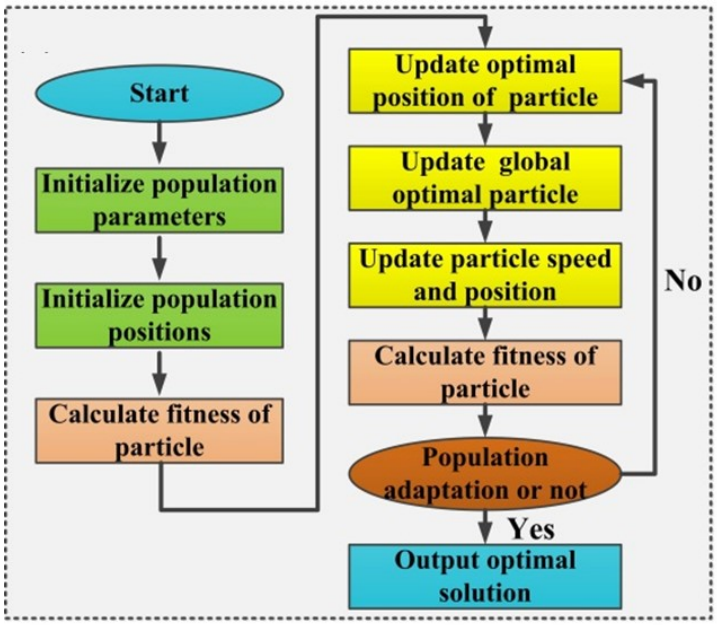

Fig. S2. The workflow diagram of the PSO algorithm

Moreover, the meta-atom library composed of six distinct meta-atoms provides a significantly expanded select space, which enables the PSO algorithm to select a meta-atom at each position optimally matching the ideal multi-frequency phase profile, thereby minimizing the overall wavefront error and maximizing the overall lens efficiency.

Supplementary Section 4: The manufacturing process of dielectric metalens

The fabrication process commences with the thorough cleaning of the SiO_2 substrate, as any residual microparticles or contaminants may induce significant defects in subsequent processing steps. Following cleaning, a thin film deposition procedure is carried out. Given the high transparency and low loss of silicon within the 1340 ~ 1540 nm wavelength range, a 1 μm thick Si layer and a 50 nm thick Cr layer are successively deposited using an electron beam evaporation (EBE) system, which is chosen for its high deposition rate, excellent film density, and minimal contamination.

The next step involves patterning the structure via electron beam lithography (EBL), where a focused electron beam exposes the photoresist and transfers the target pattern onto the substrate surface. During EBL, various exposure parameters must be carefully optimized to achieve high pattern fidelity while maintaining process efficiency.

Dry etching, applicable to materials such as Si, SiO_2, and metallic thin films, is then employed. Owing to the high etch selectivity between Cr and Si, Cr serves as an effective hard mask for fabricating high-aspect-ratio structures. In this stage, the patterned photoresist acts as an initial mask for etching the underlying Cr layer, thereby transferring the geometry from the resist to the Cr hard mask. After the Cr etching is complete, the residual photoresist is removed, leaving a Cr pattern that functions as the final mask for the subsequent dry etching of the exposed Si regions. This step ultimately transfers the pattern from the Cr hard mask into the Si thin film, completing the structural fabrication. And the flow diagram for the fabrication of metalens is depicted in Fig. S3.

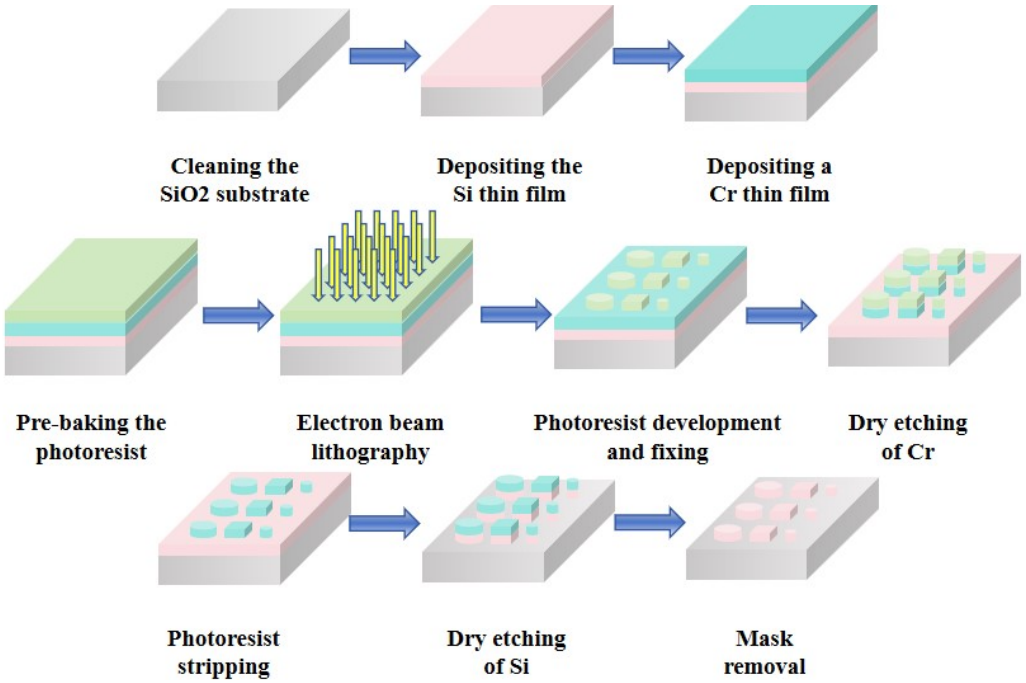

Fig. S3. Process flow diagram for the fabrication of dielectric metalens

Supplementary Section 5: The simulation results of designed metalens

The designed metalens is numerically analyzed using the FDTD method, and the resulting intensity distributions are shown in Fig. S4. Specifically, Fig. S4(a) presents the normalized intensity distribution in the *x*–*z* plane under *x*-polarization incidence at sampling wavelengths of 1.34 μm, 1.40 μm, 1.45 μm, 1.48 μm, and 1.54 μm. Fig. S4(b) shows the corresponding normalized intensity distributions under *y*-polarization incidence. It can be observed that the focal spot remains consistent and nearly overlaps in position under both polarization states, indicating that the designed metalens exhibits excellent polarization-insensitive broadband achromatic performance. Fig. S4(c) and (d) display the intensity profiles in the *x*–*y* plane for the five sampling wavelengths. Clear and bright focal spots are observed at all wavelengths, with no significant defocusing, demonstrating the robust focusing capability of the metalens across the entire sampled wavelength range.

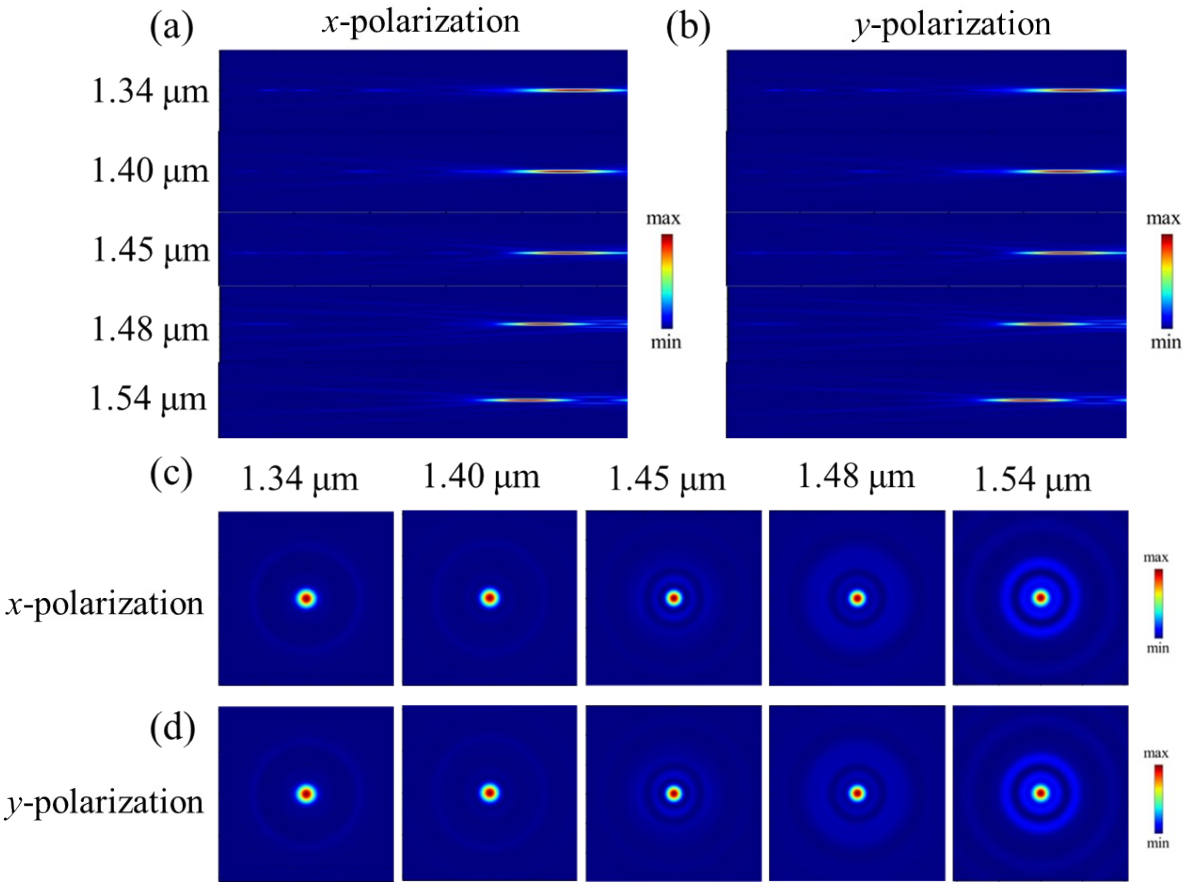

Fig. S4. Simulated normalized intensity distributions of the designed metalens. (a) *x*–*z* plane under *x*-polarization incidence; (b) *x*–*z* plane under y-polarization incidence; (c) *x*–*y* plane (focal plane) under *x*-polarization incidence; (d) *x*–*y* plane (focal plane) under *y*-polarization incidence.

Supplementary Section 6: The metalens imaging test system

Figure S5 shows the imaging experimental setup. Specifically, Figure S5(a) illustrates the schematic diagram of the imaging optical path, while Figure S5(b) displays the actual optical path used in the imaging test. It should be noted that the subscript "11" in Figure S5(a) denotes the resolution target. In this experiment, the 1951 USAF resolution test chart was employed as the object to evaluate the imaging capability of the designed metalens. The resolution target was placed at a distance of twice the focal length from the metalens. Through this optical configuration, the image formed by the metalens could ultimately be observed on the CCD.

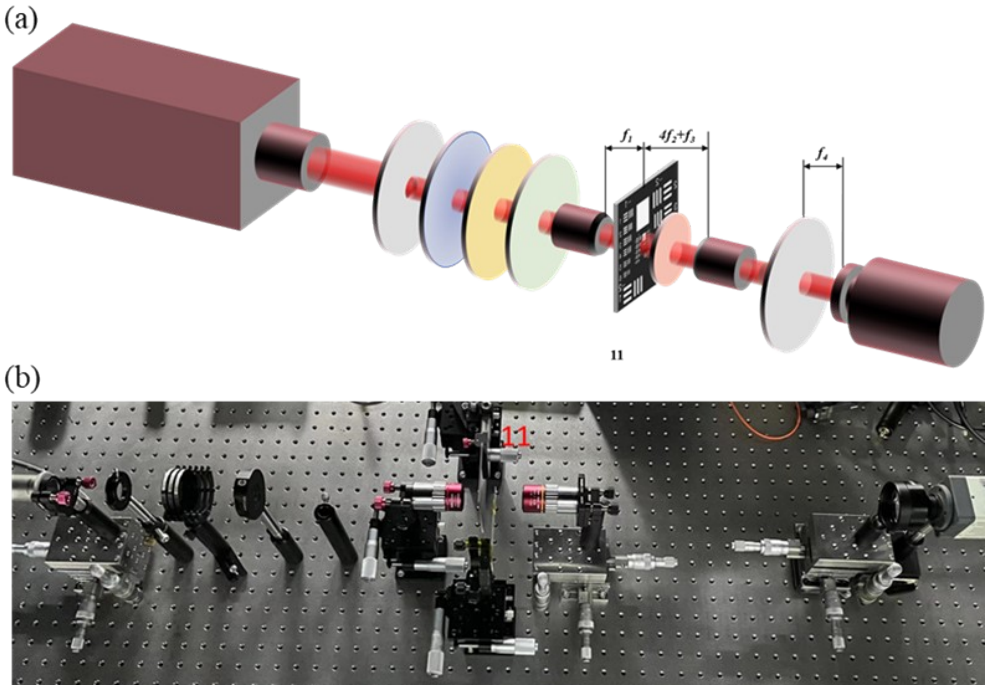

Fig. S5. Imaging characterization of the metalens. (a) Schematic diagram of the imaging optical path; (b) Experimental setup of the imaging test.

The models and key parameters of the core experimental equipment are shown in the following table.

Table S2. Literature survey of broadband achromatic metalenses in the NIR and comparison to this work.

Equipment	Model	Key Parameters
Aperture diaphragm	LBTEK DP12	Ø 1-12 mm
Narrowband Filter	Thorlabs FBH1340-12, FBH1400-12, FBH1450-12, FBH1480-12, FBH1540-12	Ø25 mm, Wavelength = 1340, 1400, 1450, 1480, 1540 nm, FWHM = 12 nm
Resolution Chart	LBTEK USAF 1951 RTS3AB-N	0.25-228 lp/mm
High-Precision 3D Displacement Stage	LBTEK LS65-13C3P	Coarse adjustment: 13 mm stroke, minimum scale 10 μm; Fine adjustment: 200 μm stroke, minimum scale 0.5 μm
Microscope objective (Beam Shrinkage)	Mitutoyo MPLNAPO5XVIR	Magnification: 5×, Focal length: 40 mm, NA: 0.14, Diameter: 3.22 cm, Wavelength range: 480-1800 nm
Microscope eyepiece (Beam Expansion)	Mitutoyo MPLNAPO10XVIR	Magnification: 10×, Focal length: 20 mm, NA: 0.26, Diameter: 3.22 cm, Wavelength range: 480-1800 nm
optical lens	LBTEK MCX20612	Diameter: 25.4 mm, Focal length: 75.3 mm
Supercontinuum Laser Source	Energetiq EQ-99X-FC	Collimated output, Wavelength range: 190-2500 nm, Power: 300 mW
CCD Camera	Hamamatsu Photonics C12741-03	640 x 512 pixels, Wavelength range: 900 - 1700 nm, Pixel size: 15 μm

Supplementary Section 7: The resolution of metalens imaging

As shown in Fig. S6, the ratio of maximum to minimum intensity in both directions is measured to be less than 1:0.735, thus confirming the achieved resolution of 19.69 μm for the designed metalens. These results demonstrate the significant potential of the proposed metalens for applications in microscopic imaging and integrated optical systems.

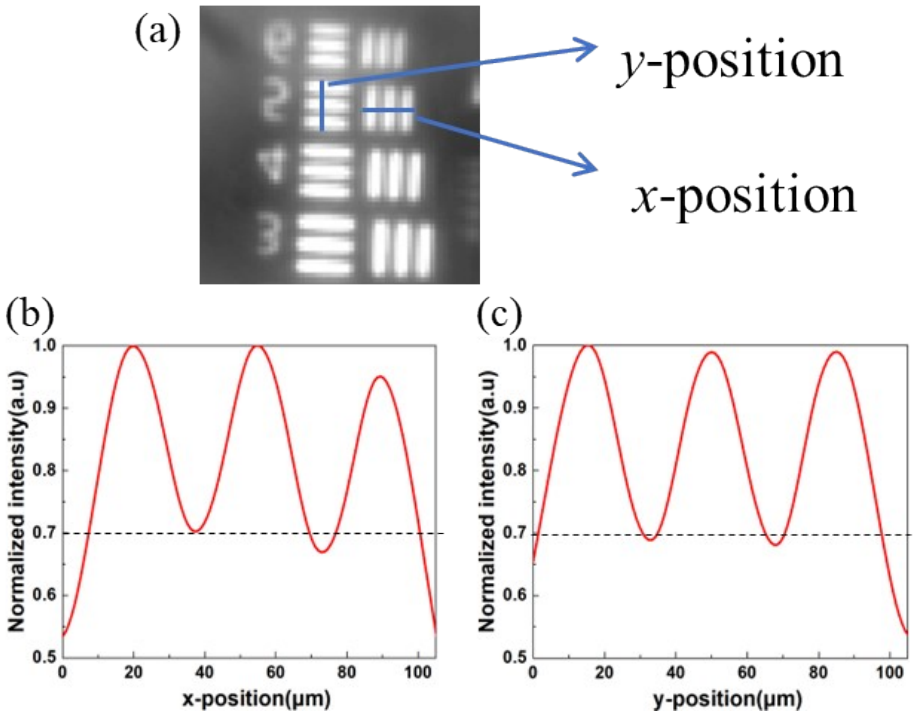

Fig. S6. (a) Broadband imaging results of the metalens across the 1.34 ~ 1.54 μm, (b)-(c) Corresponding intensity profiles along the *x* and *y* directions, respectively.

Supplementary Section 8: The focusing efficiency of metalens

The average focusing efficiency of the metalens is 18.04%, which is relatively low. In general, the reduced efficiency of achromatic metalenses stems from multiple factors. These include amplitude variations caused by inconsistent scattering efficiency among meta-units, phase errors arising from discrepancies between the required and actual phase responses, and nearest-neighbor coupling effects where adjacent structures perturb the optical response, particularly pronounced in taller meta-unit designs due to increased interaction length. Fabrication imperfections such as sidewall roughness and slope further contribute to losses. Additionally, backscattering reflects a portion of the incident energy, and parasitic focal spots divert some light to axial positions away from the intended focal point, collectively degrading the overall focusing efficiency.

Based on the factors limiting efficiency discussed above, several strategies can be pursued to further enhance the focusing efficiency of achromatic metalenses. Optimizing the meta-unit design by carefully tailoring the geometry, such as increasing the aspect ratio within fabrication limits, can achieve stronger phase modulation and lower scattering loss. Employing inverse design methods or topology optimization may help identify non-intuitive structures that simultaneously provide accurate phase coverage and high transmission. Minimizing nearest-neighbor coupling effects by optimizing the unit cell period or introducing isolation structures can reduce the influence of adjacent meta-units. Adopting a "pixel-based" design strategy that accounts for near-field coupling during the optimization process can yield more accurate optical responses and improved efficiency. Improving fabrication accuracy by reducing sidewall roughness and controlling etch slope through process refinement can significantly suppress scattering losses, and advances in nanofabrication techniques will enable more faithful reproduction of design geometries. Exploring alternative material platforms, such as titanium dioxide, gallium nitride, or barium titanate, may provide lower absorption or better refractive index contrast, potentially boosting efficiency. Finally, suppressing parasitic effects by incorporating anti-reflection layers or optimizing the impedance matching of the metasurface can mitigate backscattering, while more rigorous phase profile optimization can reduce parasitic focal spots, ensuring that most of the transmitted energy converges to the intended focal point.

Supplementary Section 9: Neural network model selection

Regarding the neural network model employed in this study, its specific source reference and key parameter configurations are detailed in the corresponding table within the main text. The relevant information is reproduced below:

Table S4. Comparison of super-resolution algorithms on benchmark datasets[1].

Dataset		nearest	bicubic	SRCNN	SelfExSR	DRCN	ESPCN	SRGAN	HR	**SRResNet**
Set5	PSNR	26.26	28.43	30.07	30.33	31.52	30.76	29.40	∞	**32.05**
	SSIM	0.7552	0.8211	0.8627	0.8720	0.8938	0.8784	0.8472	1	**0.9019**
	MOS	1.28	1.97	2.57	2.65	3.26	2.89	3.58	4.32	**3.37**
Set14	PSNR	24.64	25.99	27.18	27.45	28.02	27.66	26.02	∞	**28.49**
	SSIM	0.7100	0.7486	0.7861	0.7972	0.8074	0.8004	0.7397	1	**0.8184**
	MOS	1.20	1.80	2.26	2.34	2.84	2.52	3.72	4.32	**2.98**
BSD100	PSNR	25.02	25.94	26.68	26.83	27.21	27.02	25.16	∞	**27.58**
	SSIM	0.6606	0.6935	0.7291	0.7387	0.7493	0.7442	0.6688	1	**0.7620**
	MOS	1.11	1.47	1.87	1.89	2.12	2.01	3.56	4.46	**2.29**

In our study, due to the higher requirements for objective evaluation of image reconstruction quality, we prioritized models with better PSNR and SSIM performance during model selection, which are widely recognized as standard benchmarks for assessing the fidelity and structural similarity of reconstructed images relative to ground truth. By selecting the model that achieved higher PSNR and SSIM scores on validation datasets, we ensured that the reconstructed images maintained both high pixel-level accuracy and perceptually consistent structural details.

Conferences:

1. C. Ledig, L. Theis, F. Huszár, J. Caballero, A. Cunningham, A. Acosta, A. Aitken, A. Tejani, J. Totz, Z. Wang and W. Shi, 2017.